



## RESEARCH ARTICLE

10.1002/2016JF004061

## Intrawave sand suspension in the shoaling and surf zone of a field-scale laboratory beach

## Key Points:

- Turbulence beneath plunging waves is highly effective in stirring sand from the bed
- Sand suspension is phase coupled to the wave-orbital motion under all wave conditions
- Wave-driven suspended sand transport is onshore beneath plunging waves

## Correspondence to:

J. A. Brinkkemper,  
j.a.brinkkemper@uu.nl

## Citation:

Brinkkemper, J. A., A. T. M. de Bakker, and B. G. Ruessink (2017), Intrawave sand suspension in the shoaling and surf zone of a field-scale laboratory beach, *J. Geophys. Res. Earth Surf.*, 122, 356–370, doi:10.1002/2016JF004061.

Received 22 AUG 2016

Accepted 6 DEC 2016

Accepted article online 10 DEC 2016

Published online 25 JAN 2017

J. A. Brinkkemper<sup>1</sup> , A. T. M. de Bakker<sup>1,2</sup> , and B. G. Ruessink<sup>1</sup>

<sup>1</sup>Department of Physical Geography, Faculty of Geosciences, Utrecht University, Utrecht, Netherlands, <sup>2</sup>UMR LIENSs, CNRS Université de la Rochelle, La Rochelle, France

**Abstract** Short-wave sand transport in morphodynamic models is often based solely on the near-bed wave-orbital motion, thereby neglecting the effect of ripple-induced and surface-induced turbulence on sand transport processes. Here sand stirring was studied using measurements of the wave-orbital motion, turbulence, ripple characteristics, and sand concentration collected on a field-scale laboratory beach under conditions ranging from irregular nonbreaking waves above vortex ripples to plunging waves and bores above subdued bed forms. Turbulence and sand concentration were analyzed as individual events and in a wave phase-averaged sense. The fraction of turbulence events related to suspension events is relatively high (~50%), especially beneath plunging waves. Beneath nonbreaking waves with vortex ripples, the sand concentration close to the bed peaks right after the maximum positive wave-orbital motion and shows a marked phase lag in the vertical, although the peak in concentration at higher elevations does not shift to beyond the positive to negative flow reversal. Under plunging waves, concentration peaks beneath the wavefront without any notable phase lags in the vertical. In the inner-surf zone (bores), the sand concentration remains phase coupled to positive wave-orbital motion, but the concentration decreases with distance toward the shoreline. On the whole, our observations demonstrate that the wave-driven suspended load transport is onshore and largest beneath plunging waves, while it is small and can also be offshore beneath shoaling waves. To accurately predict wave-driven sand transport in morphodynamic models, the effect of surface-induced turbulence beneath plunging waves should thus be included.

## 1. Introduction

Short (sea or swell, 2–20 s) waves are an important sand stirring agent in the nearshore zone and largely determine the amount of suspended sand available for transport by other hydrodynamic processes, such as infragravity waves and mean currents. When sand is predominantly suspended during a particular phase of the orbital motion, short waves can also transport sand themselves [e.g., Jaffe *et al.*, 1984]. While short-wave sand transport beneath nonbreaking waves on a plane bed (i.e., sheetflow conditions) is reasonably well understood from extensive laboratory experiments, ripple-induced and surface-induced turbulence effects have not received much attention. Both can strongly affect the phase coupling between sand suspension and the wave-orbital motion in natural shoaling and surf zones, respectively. These effects are not yet represented in current morphodynamic models [e.g., Van Rijn *et al.*, 2013; Dubarbier *et al.*, 2015] and are the focus of the present paper.

In the absence of a mean cross-shore current, nonzero shortwave-induced sand transport  $Q_{hf}$  under sheet flow conditions demands the orbital motion to be nonlinear. As waves propagate toward the beach into shallower water, they become skewed (high narrow crests and low wide troughs) in the shoaling zone and asymmetric (pitched forward) in the surf zone. This shape transition leads to analogous changes in the near-bed orbital motion. Experiments with skewed flow velocities in oscillatory flow tunnels [e.g., King, 1991; Ribberink and Al-Salem, 1994; O'Donoghue and Wright, 2004] have illustrated that these flows drive positive (i.e., “onshore”) sand transport when the median grain size  $D_{50}$  is coarser than ~200  $\mu\text{m}$ , as the higher positive velocities are capable of mobilizing larger amounts of sand [e.g., Ribberink and Al-Salem, 1994] than the lower negative velocities. For finer sand, the sand has not all settled at the time of flow reversal from positive to negative directed and may therefore be transported by the negative flow. These phase-lag effects can cause  $Q_{hf}$  to become negative, i.e., “offshore” directed [Dohmen-Janssen *et al.*, 2002; O'Donoghue and Wright, 2004; Grasso *et al.*, 2011]. Below velocity-asymmetric flow, maximum positive and negative velocities are equal in

©2016. The Authors.

This is an open access article under the terms of the Creative Commons Attribution-NonCommercial-NoDerivs License, which permits use and distribution in any medium, provided the original work is properly cited, the use is non-commercial and no modifications or adaptations are made.

magnitude; however, flow tunnel experiments show these flows still drive sand transport in the positive direction [e.g., van der A *et al.*, 2010; Grasso *et al.*, 2011; Ruessink *et al.*, 2011]. The net positive-directed transport of sand by velocity-asymmetric flows can be explained by two effects. First, the time between the maximum positive velocity and the positive-negative flow reversal is longer than the time between the maximum negative and the negative-positive flow reversal. This means that sand suspended during the maximum negative velocity has less time to settle prior to flow reversal and is prone to be moved in the positive direction. Numerical simulations by Ruessink *et al.* [2009] indicate that this effect only contributes to the net transport when  $D_{50} \lesssim 250 \mu\text{m}$ . Second, the high acceleration from negative to positive flow induces high bed shear stresses [Nielsen, 1992], as the boundary layer has limited time to grow, in comparison with a longer time span and low acceleration during the change from positive to negative flow. This causes the suspension peak during positive flow to just exceed that during negative flow [Ruessink *et al.*, 2011], and thus,  $Q_{hf}$  is small but positive.

The presence of ripples in the sea bed complicates the short-wave sand transport considerably. Measurements by Ribberink and Al-Salem [1994] in an oscillatory flow tunnel showed a reduction in the positive-directed suspended sand transport in the presence of ripples. Several other laboratory [e.g., van der Werf *et al.*, 2007] and field [e.g., Osborne and Vincent, 1996] studies showed that steep vortex ripples can even cause a reversal in the net transport direction to offshore [see also Aagaard *et al.*, 2013]. This influence of vortex ripples is caused by turbulent vortices that are ejected from the ripple crests during flow reversal. During positive flow velocities, a vortex is formed at the lee side of the ripple crest, which detaches from the bed during flow reversal from positive to negative velocities, and is subsequently ejected into the water column during the negative flow phase. This phenomenon also occurs during the negative-positive flow reversal, but due to the higher positive velocities under velocity-skewed flows the ejected vortex at positive-negative flow reversal is larger and, as a result, suspended sand is transported in the net negative direction. The sand concentration above vortex ripples is thus both variable in time and space, and suspended transport estimates highly depend on the location with respect to the ripple crest [e.g., Osborne and Vincent, 1996; Thorne *et al.*, 2003; van der Werf *et al.*, 2007].

Surface-induced turbulence injected by breaking waves is another mechanism that can affect the phase coupling between sand suspension and orbital flow. Depending on the breaker type and the stage of breaking, turbulence is organized in obliquely descending eddies (ODEs), horizontal vortices, or both [Nadaoka *et al.*, 1989; Zhang and Sunamura, 1990]. ODEs, which are observed beneath spilling breakers and bores [Zhang and Sunamura, 1990], intermittently descend toward the bed and suspend sand [Nadaoka *et al.*, 1988]. Yoon and Cox [2012] found that 20–35% of the turbulence events beneath spilling breakers resulted in a suspension event and concluded that most of the turbulence dissipated before it reached the bed. These events did, however, explain 50–65% of the observed suspension events. The turbulence field beneath plunging breakers is characterized by an injection of turbulence at the plunge point, the location where the plunging jet hits the water surface, and the formation of large-scale horizontal vortices at the wavefront. These turbulent structures are more effective in stirring sand from the bed than the vortices beneath spilling breakers [e.g., Beach and Sternberg, 1996; Aagaard and Hughes, 2010]. Moreover, the large-scale horizontal vortices enable the sand to be mixed throughout the water column. Whether the additional sand stirred from the bed by wave breaking induced turbulence affects the magnitude or direction of the short-wave sand transport depends on the timing of sand stirring in respect to the wave phase. Several studies suggest that sand stirring in the surf zone becomes unrelated with the wave-orbital motion and  $Q_{hf}$  thus reduces to zero [Sato *et al.*, 1990; Barkaszi and Dally, 1992; Nadaoka *et al.*, 1988]. Other laboratory and field studies suggest, however, that  $Q_{hf}$  in the surf zone can either be positive [e.g., Jaffe and Sallenger Jr., 1992; van Thiel de Vries *et al.*, 2008; Aagaard and Hughes, 2010] or negative [e.g., Scott *et al.*, 2009].

The main goal of this study is to gain more insight in the effect of the surface-induced turbulence on sand suspension beneath plunging breaking waves. More specifically, our steps are (1) to quantify the effectiveness of turbulence events in stirring sand from the bed and (2) to determine the phase coupling of sand suspension to the wave-orbital motion, beneath nonbreaking waves, plunging breaking waves and bores. Understanding this effect is crucial to be able to predict sand transport by short waves in the surf zone and to eventually improve morphodynamic models. In this study, field-scale flume measurements collected during the Barrier Dynamic Experiment II (BARDEXII) were used. This experiment gave us the opportunity to simulate field-like conditions, with the advantage of more detailed measurements (i.e., more sensors and very detailed bed

surveys) and more control over instrument heights. The first mentioned goal was approached by determining the fraction of related turbulence and suspension events. To reach the second goal, the focus was on the timing of sand suspension in the wave-orbital motion as this largely determines the magnitude and direction of the short-wave transport. The paper is structured as follows. In section 2 the laboratory experiments, data processing, and analysis procedures are described. Subsequently, in section 3, the results from the event-based approach and the wave phase-based approach are presented. A discussion of the results is found in section 4, and the main conclusions of our work are provided in section 5.

## 2. Methods

### 2.1. Data Collection

The Barrier Dynamic Experiment II (BARDEXII) was conducted in the Delta flume in Vollenhove, The Netherlands, in 2012 [Masselink *et al.*, 2016]. The initial bed profile consisted of a 4.5 m high, 5 m wide, and 75 m long sandy (median grain diameter  $D_{50} = 430 \mu\text{m}$ , mean grain size = 510  $\mu\text{m}$ ) barrier. The initial beach slope was 1:15 from  $x = 49 \text{ m}$  to  $x = 109 \text{ m}$ , where  $x = 0 \text{ m}$  is the wave maker (Figure 1). The experiment consisted of five series (A–E) that were divided into tests with different wave and/or water level conditions. Each test was subsequently divided into wave runs with a duration of 10 to 120 min; between runs the bed level along the entire flume was surveyed [Ruessink *et al.*, 2016]. This study focuses on the tests that were designed to study surf-swash dynamics, i.e., tests A1–C2. During these tests, irregular waves with test-dependent offshore significant wave height  $H_s$  and peak period  $T_p$  (Table 1) were forced using a JONSWAP spectrum. During series A, the beach profile was first (A1–A4) subjected to erosive waves ( $H_s = 0.8 \text{ m}$ ,  $T_p = 8 \text{ s}$ ), causing sand to be eroded from the inner-surf zone to form a sandbar in the outer-surf zone [Ruessink *et al.*, 2016]. In the second part (A6–A8), accretive waves ( $H_s = 0.6 \text{ m}$ ,  $T_p = 12 \text{ s}$ ) resulted in the migration of the sandbar in the onshore direction, until it eventually merged with the beach face to form a steep (1:6) berm [Ruessink *et al.*, 2016]. Series B consisted of two tests with a different water level ( $\zeta = 3$  and  $\zeta = 2.5 \text{ m}$ , where  $\zeta$  refers to the height of the still water above the concrete flume floor). In series C a tidal cycle was simulated by raising (C1) and subsequent lowering (C2) of the water level in steps of maximum 0.2 m between wave runs. The sandbar remained relatively stable during series B and C [Ruessink *et al.*, 2016], see also Figure 1.

Concurrent suspended sand concentration and velocity measurements, of which the latter suitable to quantify turbulence characteristics, were collected using a rig deployed at  $x = 65 \text{ m}$  (Figure 1). The Turbulence-Rig (TR hereafter) contained three sideways oriented Ocean Acoustic Doppler Velocimeters (ADVOs) measuring flow velocity in all directions at 10 Hz, a vertical array of 7 Seapoint Turbidity Meters (STMs) to estimate suspended sand concentrations (4 Hz) and a Pressure Transducer (PT) to sample near-bed pressure (4 Hz). The height of the rig was manually adjustable, ensuring an equal height of the instruments above the bed at the start of each wave run (0.175, 0.435, and 0.7 m for ADV1–3; 0.04, 0.07, 0.10, 0.14, 0.17, 0.44, and 0.71 m for STM1–7; and 0.25 m for the PT). The horizontal distance between the instruments and the nearest flume wall was around 2 m.

Additional velocity and suspension data were collected using three rigs (R1, R2, and R3) at  $x = 60$ ,  $x = 70$ , and  $x = 75 \text{ m}$  (Figure 1). These rigs contained an electromagnetic flow meter at  $z \approx 0.11 \text{ m}$  to measure flow velocities in the cross-shore and alongshore directions, a vertical array of 3 STMs ( $z \approx 0.04$ , 0.06, and 0.11 m) and a PT ( $z \approx 0.25 \text{ m}$ ). Although turbulence could not be estimated at these locations, these measurements do enable us to analyze the phase coupling between the orbital motion and sand concentration at multiple cross-shore locations. Pressure transducers were also deployed individually at nine locations (Figure 1).

The bed elevation was measured using a mechanical bed profiler (cross-shore resolution of 0.01 m) in between each wave run along the centerline of the flume to quantify both the large-scale bar-berm and small-scale wave ripple morphology. Additionally, a 3-D Profiling Sonar was deployed at  $x = 63.1 \text{ m}$  to obtain circular elevation models of small-scale bed forms in between wave runs and information on ripple migration during the runs [Ruessink *et al.*, 2015]. Moreover, three Argus type cameras were deployed [Masselink *et al.*, 2016] to collect information on the location of wave breaking. Breaking waves generate white foam and are therefore easily recognized on these images. The pixel intensity along the centerline of the flume was averaged over a 50 pixel wide “alongshore” strip and subsequently collected in a timestack. It was chosen to average over a certain amount of pixels rather than a fixed part of the flume width, as the purpose was to reduce pixel noise (the water surface is considered homogeneous over the width of the flume).

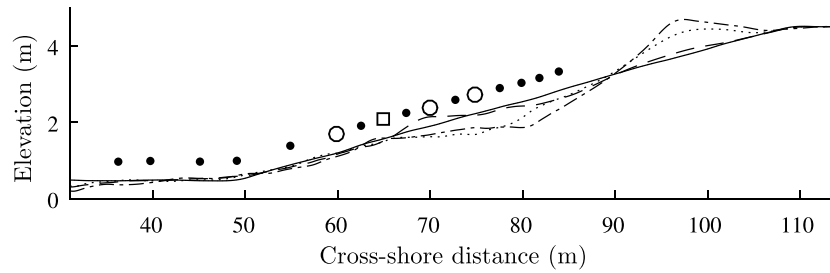


**Figure 1.** The (solid) initial profile and profiles after (dashed line) A4, (dotted line) A8, and (dash-dotted line) C2. The location of the instrument rigs, (square) TR, and (circles, numbered in positive x axis direction) R1, R2, and R3 are indicated, as well as the location of the (dots) individual pressure transducers.

### 2.2. Data Processing

Instantaneous pressure time series were converted to water surface elevation using linear wave theory. The water depth ( $h$ ) was calculated as the sum of the instrument height above the bed with the mean of the pressure time series. The instantaneous water surface elevation was bandpass filtered to obtain the short-wave part ( $\eta_{hf}$ ) with  $0.05 < f < 1$  Hz and processed into the significant short-wave height ( $H_s$ ). The nonlinearity of the short waves was expressed with the skewness ( $Sk$ ) and asymmetry ( $As$ ) as

$$Sk = \frac{\langle \eta_{hf}^3 \rangle}{\langle \eta_{hf}^2 \rangle^{3/2}} \tag{1}$$

$$As = \frac{\langle (H(\eta_{hf}))^3 \rangle}{\langle \eta_{hf}^2 \rangle^{3/2}} \tag{2}$$

where  $H$  denotes the Hilbert transform [Elgar, 1987].

The velocity series from the ADVs were quality controlled and despiked based on the guidelines provided in Elgar et al. [2005] and Mori et al. [2007]. Beam velocities were transformed into the ADV's orthogonal coordinate system and subsequently rotated into cross-shore  $u$ , alongshore  $v$  (wall to wall) and vertical  $w$  velocities. Positive  $u$  is in the shoreward direction, positive  $v$  is into the sensor perpendicular to the flume, and positive  $w$  is upward. Further details on the quality control measures applied on the velocity measurements are described in Ruessink [2010]. The turbulence velocities  $u'$ ,  $v'$ , and  $w'$  were estimated using the two-sensor filtering technique developed by Feddersen and Williams [2007] and modified by Gerbi et al. [2009]. This method uses adaptive-filtered velocities from a vertically spaced sensor B to estimate the turbulence at sensor A, denoted A(B), where A and B can be ADV 1, 2, or 3. To reduce bias in the turbulence velocities due to wave damping near the bed, the sensor combinations with a relatively small vertical separation distance 1(2), 2(3), and 3(2) were chosen for the two-sensor filtering technique [Brinkkemper et al., 2016]. The turbulence velocities were combined into the instantaneous turbulent kinetic energy as

$$k = 0.5(u'^2 + v'^2 + w'^2). \tag{3}$$

**Table 1.** Hydrodynamic Conditions A–C During the BARDEXII Experiment

Test	$H_s$ (m)	$T_p$ (s)	$\zeta$ (m)	$Q_b$ ( $x = 65$ m)
A1	0.89	8	3	0.07
A2	0.88	8	3	0.09
A3	0.88	8	3	0.07
A4	0.88	8	3	0.11
A6	0.69	12	3	0.01
A7	0.77	12	3	0.05
A8	0.77	12	3	0.04
B1	0.89	8	3	0.03–0.08
B2	0.87	8	2.5	0.17–0.26
C1	0.88,0.55	8	2.25–3.65	0.41–0
C2	0.55,0.90	8	3.53–2.25	0–0.48

The STMs were postcalibrated in a recirculation tank using sand samples collected at the locations of the instrument rigs at the end of the experiment. The output of the instruments correlated quadratically with the sand concentration over the range 0–40 kg/m<sup>3</sup> ( $r^2 \geq 0.99$  for all instruments). Small background concentrations were removed by subtracting the 0.5 percentile in blocks of 15 min. Concentration signals that indicated instrument burial in the bed or the presence of bubbles were rejected. Air bubbles beneath breaking waves and surf zone bores can have a significant effect on measurements recorded by optical instruments [Puleo *et al.*, 2006]. In the time series these bubbles can be recognized as a steep spike in concentration, often occurring prior to an actual sand suspension event. Time series were rejected when a cross correlation with the concentration signal at a lower sensor resulted in a negative phase lag, i.e., when concentration peaked earlier at a higher than lower sensor, and when the mean in sand concentration decreased toward the bed [e.g., Aagaard and Jensen, 2013].

Ripples were separated from the large-scale morphology by applying a second-order loess interpolator [Plant *et al.*, 2002] with  $l_x = 3.5$  m. This acts as a high-pass filter and removes variability with length scales larger than  $l_x/0.7$  (i.e., 5 m). The cross-shore ripple statistics, ripple height ( $\eta_r$ ), ripple length ( $\lambda_r$ ), and ripple steepness ( $\theta_r = \eta_r/\lambda_r$ ) were calculated every 0.5 m from overlapping (95%) windows with a length of 10 m. As this approach occasionally resulted in unrealistically large variations in ripple statistics in especially the breaker zone, the statistics were low-pass filtered with  $l_x = 3.5$  m. The computation of ripple statistics from the collected bed profiles was described in more detail by Ruessink *et al.* [2015].

The video timestacks were used to identify the location where individual waves were breaking, as this is clearly visible in timestacks due to the white foam that is generated shortly after a plunging jet hits the water surface. The fraction of broken waves ( $Q_b$ ) was consequently determined at the location of each instrument rig and for each wave run, as the amount of broken waves at these locations divided by the total amount of waves. See Brinkkemper *et al.* [2016] for further details.

## 2.3. Data Analysis

### 2.3.1. Related Events

Turbulence measurements from the lowest ADVO ( $z \approx 0.175$  m) and the concentration measurements from the lowest five STMs at TR were used for the event analysis. Measurements were cut into 15 min long blocks to ensure an equal length for all time series. The readings from the lowest five STMs were combined into an instantaneous suspended load by integrating the time series, using the trapezoidal method, over the vertical distance from the lowest sensor ( $z \approx 0.04$  m) to the fifth sensor ( $z \approx 0.17$  m) [Butt *et al.*, 2004; Puleo, 2009; Yoon and Cox, 2012]:

$$C = \int_{0.04\text{ m}}^{0.17\text{ m}} c(z) dz, \quad (4)$$

where  $c(z)$  is the measured sand concentration at height  $z$  above the bed. A 2 s moving average filter was applied to smoothen both instantaneous  $k$  and  $C$  as to make the event statistics more robust. Subsequently, moderate and intense events were identified in the  $k$  and  $C$  series. Moderate  $k$  events were identified where  $k$  exceeded  $\bar{k} + \sigma$ , where  $\bar{k}$  is the series mean and  $\sigma$  is the standard deviation, but did not exceed  $\bar{k} + 3\sigma$ ; intense events were identified where  $\bar{k} + 3\sigma$  was exceeded. Moderate and intense events in the suspended load time series were identified analogously.

The fraction of time where  $k$  was above the threshold ( $\phi_k$ ) was calculated as the number of data points where the threshold was exceeded divided by the total length of the time series. The importance of the events for the total turbulent kinetic energy ( $\phi_k$ ) was calculated as the sum of values above the threshold divided by the total sum [Yoon and Cox, 2012]. The same approach was used to quantify the fraction and importance of events in the suspended load time series, with  $\phi_C$  and  $\phi_C$ .

To study which fraction of the measured suspension events was related to a turbulence event and vice versa, the fraction of related events was calculated. For this analysis, events were selected that exceeded the turbulence threshold  $\bar{k} + \sigma$  or  $\bar{C} + \sigma$  for the suspended load series. Turbulence or suspension events were identified as related when they occurred simultaneously within the time window  $\pm T_p/2$ , where  $T_p$  is the peak wave period, of a suspension or turbulence peak, respectively. Events that are advected by the wave-orbital motion can also be related by using this time window [Yoon and Cox, 2012]. The fraction of turbulence events related to

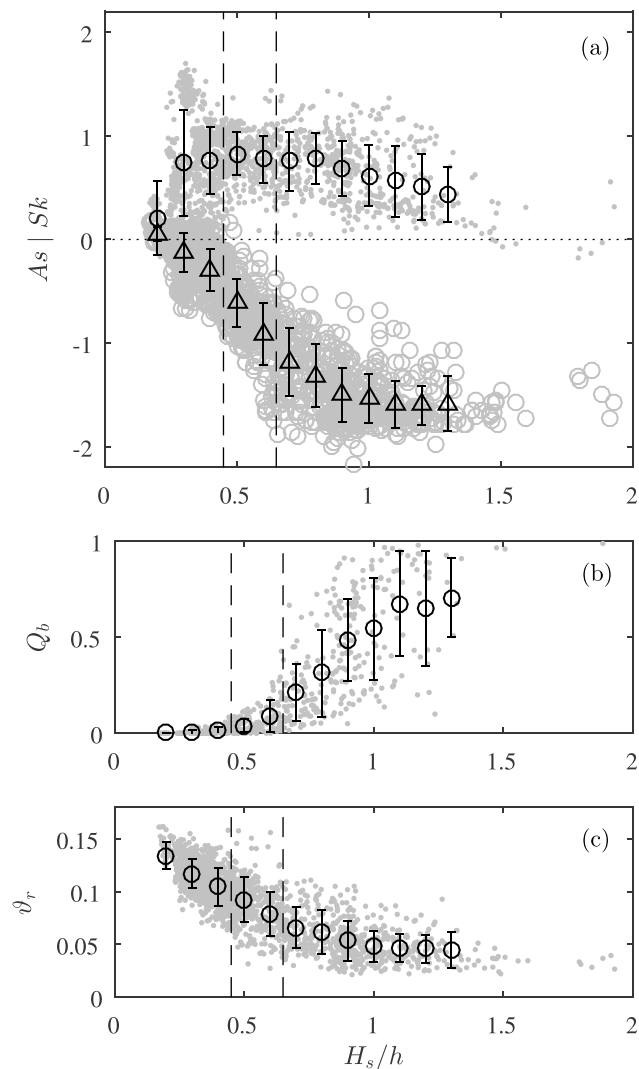


**Figure 2.** Wave shape (a) skewness  $Sk$  (dots) and asymmetry  $As$  (circles), (b) fraction of broken waves  $Q_b$ , and (c) ripple steepness  $\phi_r$  versus relative wave height  $H_s/h$  at all instrument locations. The error bars show the mean and standard deviations.

suspension events ( $E_{k|k}$ ) was calculated as  $nE_{kC}/nE_k$ , where  $nE_k$  is the amount of turbulence events and  $nE_{kC}$  is the amount of related events. Similarly, the fraction of suspension events related to turbulence events is  $E_{k|C} = nE_{kC}/nE_C$ .

### 2.3.2. Phase Coupling

While event analysis was applied for TR only, the phase-coupling analysis also included measurements collected at R1, R2, and R3. This analysis was applied for conditions C1 and C2, as the simulated tidal cycle resulted in a wide range in  $H_s/h$  at the location of the rigs, see section 2.4. The cross-shore velocity collected at TR by the lowest ADV0 was downsampled to 4 Hz to obtain a frequency equal to the concentration measurements. This downsampled signal and the cross-shore velocity measured at R1, R2, and R3 were detrended and subsequently bandpass filtered (0.05–1 Hz) to obtain the high-frequency part ( $u_{hf}$ ).

To estimate phase-averaged values of  $k$ ,  $c$ , and  $u_{hf}$ , individual waves were first identified in  $u_{hf}$  using a zero up-crossing method. Subsequently, the time axis of each wave was normalized with its period ( $t/T$ ). Time series of  $k$ ,  $c$ , and  $u_{hf}$  were then bin averaged over  $t/T$ , only including the one third highest waves, with a bin width of 0.05. Including all waves in the binning did not notably change the phase-averaged patterns presented in section 3.2.

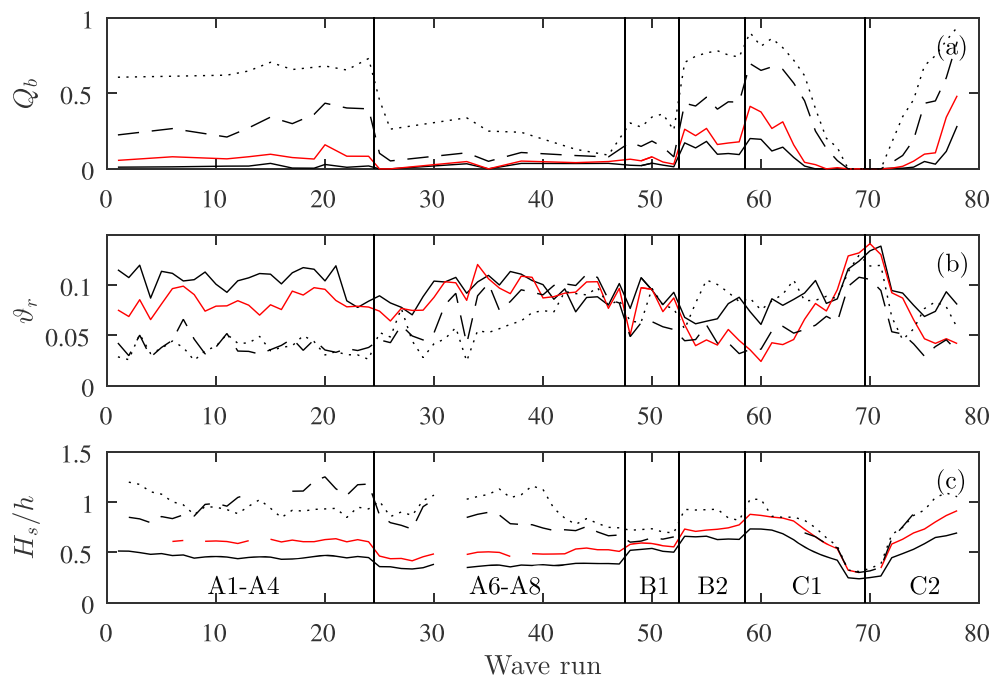


**Figure 3.** (a) Fraction of broken waves  $Q_b$ , (b) ripple steepness  $\vartheta_r$  and (c) relative wave height  $H_s/h$  at the location of the four rigs: R1 (black solid line), TR (red solid line), R2 (dashed line), and R3 (dotted line). The solid vertical lines show the separation between the test cases.

The short-wave sand transport rate at individual STMs was estimated as  $q_{hf} = \langle u_{hf} \cdot c_{hf} \rangle$ , where  $\langle \dots \rangle$  denotes the time average. The vertically integrated sand transport rate was calculated as  $Q_{hf} = \langle u_{hf} \cdot C_{hf} \rangle$ , where  $C_{hf}$  is the high-frequency part of the sand concentration integrated over the lowest 3 STMs, similar to equation (4).

**2.4. Measurement Conditions**

Due to the variability in water level, wave height, and wave period, measurements were collected under a wide range of hydrodynamic conditions, from symmetric nonbreaking waves to velocity-skewed and velocity-asymmetric breaking waves. The relative wave height ( $H_s/h$ ) has often been used to scale hydrodynamic conditions [e.g., Osborne and Greenwood, 1992; Ruessink et al., 1998; Aagaard et al., 2013], as it gives a good approximation of the location relative to the breaker zone and thus of the nonlinearity of the short waves. This approximation also holds for the Bardexll data set, as illustrated by the variability of  $S_k$  and  $A_s$  with  $H_s/h$  at the 13 pressure sensors (Figure 2) and shown by Brinkkemper et al. [2016].  $S_k$  and  $A_s$  increased with  $H_s/h$  and  $Q_b$  remained close to zero (Figure 2b) for  $H_s/h < 0.45$  (Figure 2a), which implies that these measurements were collected in the shoaling zone. The ripple steepness for these conditions was between 0.1 and 0.15 (Figure 2c), i.e., vortex ripples. As  $H_s/h$  increased from 0.45 to 0.65, the asymmetry further increased but the skewness remained constant. This  $H_s/h$  range is the transition from the shoaling to the surf zone. When  $H_s/h > 0.65$ , instruments were located in the surf zone, with  $|A_s| > S_k$  and an increasing  $Q_b$ . Under these conditions the ripples became flat and elongated, reflected in a decreasing  $\vartheta_r$  (Figure 2c). Ruessink et al. [2015] analyzed 3-D sonar scans collected during the same experiment and showed also an increase in the 3-D ripple irregularity when  $H_s/h$  increased. The increase of  $Q_b$  with  $H_s/h$  was also apparent from the turbulence magnitude, as de Winter et al. [2013] and Brinkkemper et al. [2016] showed the increase of the time-averaged turbulent kinetic energy with  $H_s/h$  for this data set, especially when  $H_s/h > 0.65$ . Besides the magnitude also the vertical turbulence profile changed, from an increase toward the bottom under nonbreaking waves to an increase both toward the bottom and to the surface beneath breaking waves. This indicates that the relative importance of surface-generated turbulence increased with  $H_s/h$ . As all these hydrodynamic parameters scale well with  $H_s/h$  and the value of  $H_s/h$  is relatively easy to estimate, this ratio was used to compare hydrodynamic conditions in this study.

An overview of measured conditions during tests A1–C2 at the location of the four rigs is presented in Figure 3. Values for  $H_s/h$  and  $Q_b$  increased over the crest of the bar (located just seaward of R3, Figure 1) during the

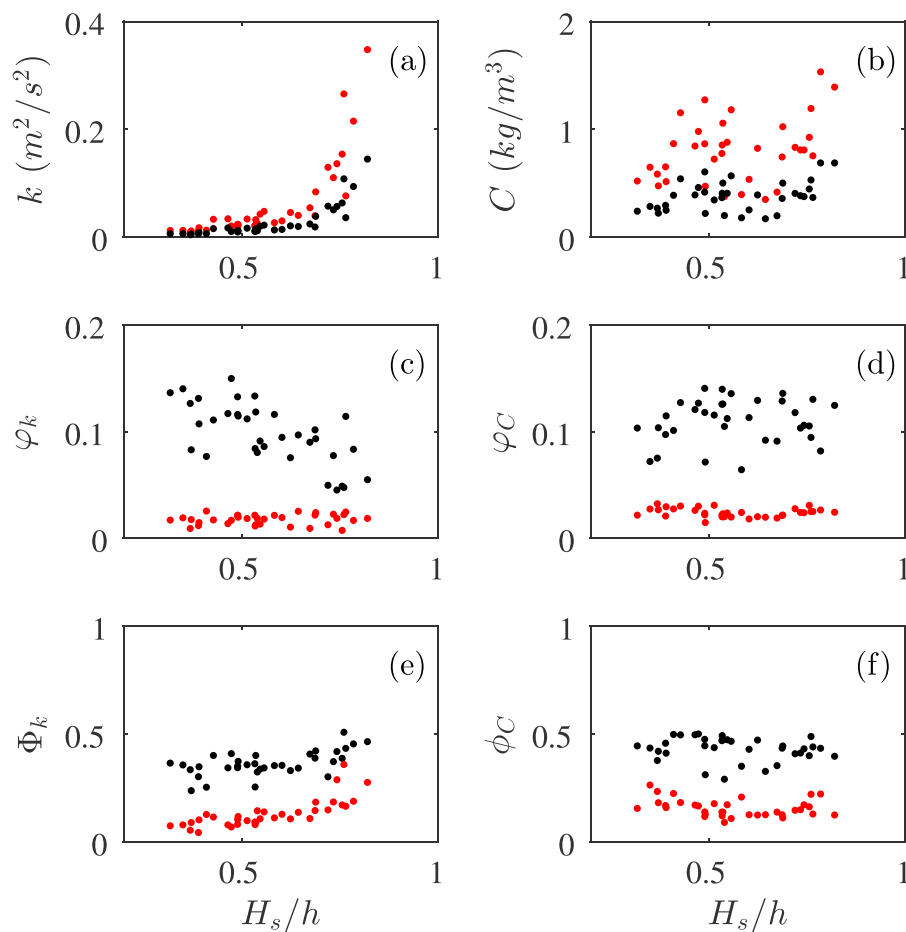


**Figure 4.** Event (a, b) thresholds, (c, d) fraction of time, and (e, f) fraction of total movement for turbulence (Figures 4a, 4c, and 4e) and suspension versus relative wave height (Figures 4b, 4d, and 4f). The black dots represent moderate events (mean +  $\sigma$ ), and the red dots represent intense events (mean +  $3\sigma$ ).

erosive conditions A1–A4 (Figures 3a and 3c). In accordance to the previous analysis, the ripples became subdued when breaking increased. During subsequent conditions (A6–A8) sand was transported toward the beach face and the water depth increased at all rigs (Figure 1), which resulted in a continuously decreasing  $Q_b$  and  $H_s/h$  at the most landward rig R3 (Figures 3a and 3c). The wave conditions during B1 were equal to the conditions during A1–A4, but the low flat terrace caused by tests A6–A8 resulted in a lower  $Q_b$  at R2 and R3. The decrease in water level during B2 raised  $H_s/h$  and  $Q_b$  at all locations. During B2,  $\vartheta_r$  was on average higher in the inner-surf zone ( $\vartheta_r \sim 0.1$ ,  $Q_b \sim 0.75$ ) than in the outer-surf zone ( $\vartheta_r \sim 0.05$ ,  $Q_b \sim 0.45$ ), as observed earlier by Ruessink *et al.* [2015].

The simulated tidal cycle during tests C1 and C2 caused  $H_s/h$  to vary between 0.3 and 1.0 (Figure 3c) and thus to cover a wide range in hydrodynamic conditions. For this reason the C series were selected to analyze phase coupling between  $c$  and  $u_{hf}$ . During the runs with  $\zeta = 2.25$  m,  $Q_b$  increased from 0.2 to 0.9 over the distance where the rigs were located. During the runs with a high water level, however, most waves broke shoreward of our instrument transect (Figure 3a). Observed ripples ranged from steep vortex ripples ( $\vartheta_r \approx 0.15$ ) beneath nonbreaking waves to hummock-type features ( $\vartheta_r \approx 0.02 - 0.03$ ) below breaking waves (Figure 3b), see Ruessink *et al.* [2015] for further details.

### 3. Results

#### 3.1. Event Statistics

Figure 4 shows the thresholds that were used to identify events and the importance of events for the total turbulence and suspension. The two thresholds for  $k$ ,  $\bar{k} + \sigma$  and  $\bar{k} + 3\sigma$ , show an exponential increase with  $H_s/h$  (Figure 4a). Thresholds for  $C$  are, in contrast, relatively constant (Figure 4b). The concentration series were

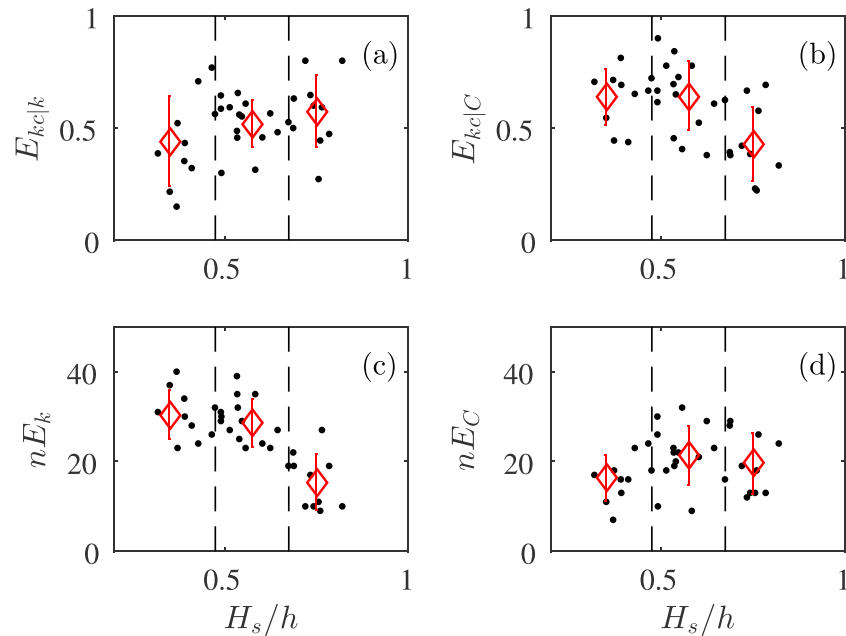


**Figure 5.** (a, b) Event correlation and (c, d) amount of events versus relative wave height ( $H_s/h$ ). The dashed lines represent the nonbreaking regime ( $H_s/h < 0.45$ ) and breaking regime ( $H_s/h > 0.65$ ). The red diamonds show the mean values and standard deviation per regime.

above the threshold  $\bar{C} + \sigma$  for about 10% of the time and above  $\bar{C} + 3\sigma$  for about 2% of the time irrespective of  $H_s/h$  (Figure 4d), while the importance of these events in the cumulative load ( $\phi_C$ ) was around 40% and 20%, respectively (Figure 4f), similar to values found in earlier studies [Yoon and Cox, 2012; Cox and Kobayashi, 2000]. The statistics for the occurrence and importance of turbulence events are comparable with the suspension event statistics (Figures 4c and 4e). However, when looking in more detail, the fraction of time when  $k$  is above the threshold ( $\phi_k$ ) decreases with  $H_s/h$  for the moderate events and approaches the values of the intense events at  $H_s/h \approx 0.8$ . This is the result of an increase in kurtosis in  $k$  with  $H_s/h$ : less threshold exceeding events are present but the events are more energetic, and thus events that exceed  $k + \sigma$  are more likely to also exceed  $\bar{k} + 3\sigma$ . While the fraction of time in which events are present decreases, the contribution of the events to the total amount of turbulence ( $\phi_k$ ) slightly increases with  $H_s/h$ , from  $<10\%$  at  $H_s/h = 0.4$  to around 20% at  $H_s/h = 0.8$  (Figure 4e).

The decrease in the fraction of time where  $k$  exceeds  $\bar{k} + \sigma$  is also reflected in the amount of detected turbulence events (Figure 5c). While the amount of events is decreasing with  $H_s/h$ , the fraction of turbulence events which is associated with a suspension event ( $E_{k|k}$ ) within  $-T_p/2$  and  $+T_p/2$  is slightly increasing (Figure 5a) from 0.4 to 0.6. This implies that turbulence events beneath breaking waves have a higher chance to generate a suspension event than the less energetic turbulence events beneath nonbreaking waves. The number of suspension events is relatively constant (Figure 5d), showing the similarity again between measured suspension signals beneath nonbreaking and breaking waves. The fraction of suspension events that are related to a turbulence event ( $E_{k|C}$ ) shows a slight decrease with increasing  $H_s/h$  (Figure 5b).

### 3.2. Phase Coupling

In the previous section it appeared that measured concentrations cannot be entirely explained by measured turbulence with an event-based approach; therefore, subsequent analysis focused on the coupling of turbulence and suspension in the wave phase. Measured sand concentrations during C1 and C2 at two heights ( $z \approx 0.04$  m and  $z \approx 0.13$  m) above the bed and at the four rig locations were wave phase-averaged per wave run (25 min). Subsequently, these phase-averaged concentrations were normalized per wave run by dividing them by their maximum value and sorted by relative wave height in Figure 6. Beneath nonbreaking waves ( $H_s/h < 0.45$ ) phase-averaged  $c$  peaks around  $t/T = 0.3$  at  $z \approx 0.04$  m, and a phase lag is observed at the higher sensor with a peak around  $t/T = 0.5$ . The increase in phase lag between  $u_{hf}$  and  $c$  in the vertical, from approximately 0.1 to 0.3 between 0.04 and 0.14 m above the bed, can be seen in more detail when

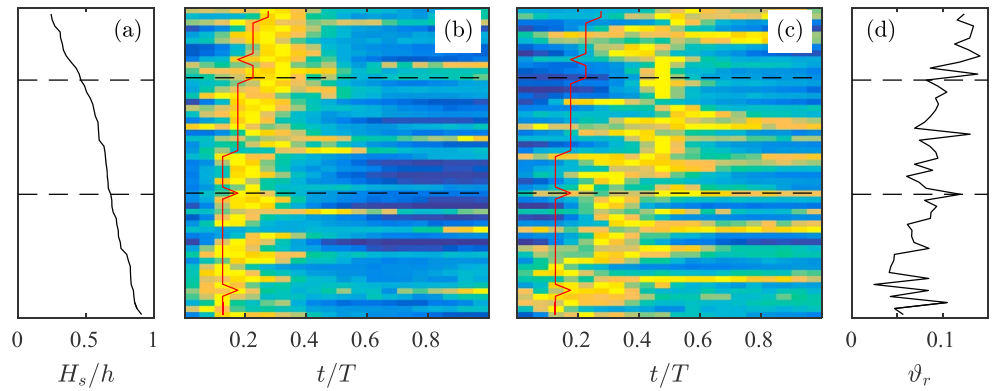


**Figure 6.** Normalized phase-averaged sand concentration from (blue) 0 to (yellow) 1, sorted by relative wave height  $H_s/h$  and measured at (b)  $z \approx 0.04$  m and (c)  $z \approx 0.11$  m. The relative wave height increases from (a) top to bottom. The red solid lines in Figures 6b and 6c indicate the timing of the maximum positive cross-shore velocity. (d) The ripple steepness  $\vartheta_r$ .

studying a nonbreaking case at the location of TR, where five vertically spaced sensors are located within this range (Figure 7e). Phase-averaged  $k$  peaks around the same  $t/T$  as phase-averaged  $c$  at the same elevation (Figure 7c), which suggests sand is suspended within turbulent vortices from the bed. Although observations show vortex-type ripples under these conditions (section 2.4), phase-averaged concentration does not show signs of ejected vortices during the negative to positive flow reversal. Whether vortex shedding is of

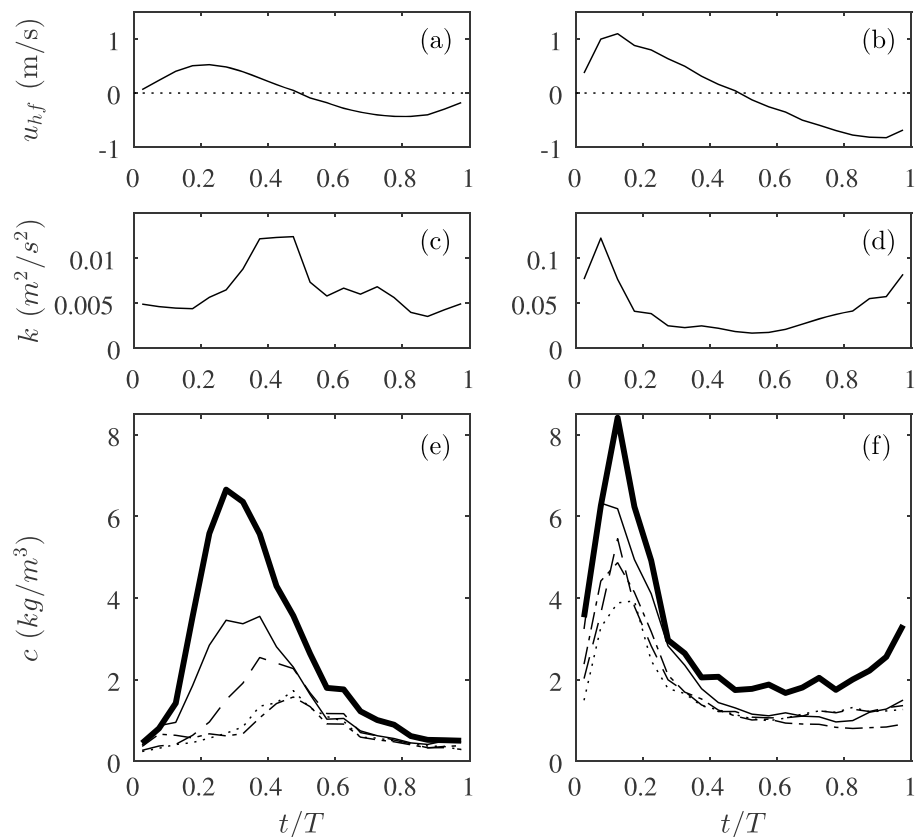


**Figure 7.** Wave phase-averaged values of (a, b)  $u_{hf}$ , (c, d)  $k$ , and (e, f)  $c$ , for a run without breaking waves (Figures 7a, 7c, and 7e) and a run with fraction of breaking waves  $Q_b \approx 0.4$  (Figures 7b, 7d, and 7f). In Figures 7e and 7f the concentrations at  $z \approx 0.04, 0.07, 0.10, 0.14,$  and  $0.17$  m are represented as thick, solid, dashed, dashed-dotted and dotted lines, respectively. In Figures 7c and 7d the turbulence at  $z \approx 0.17$  m is shown.

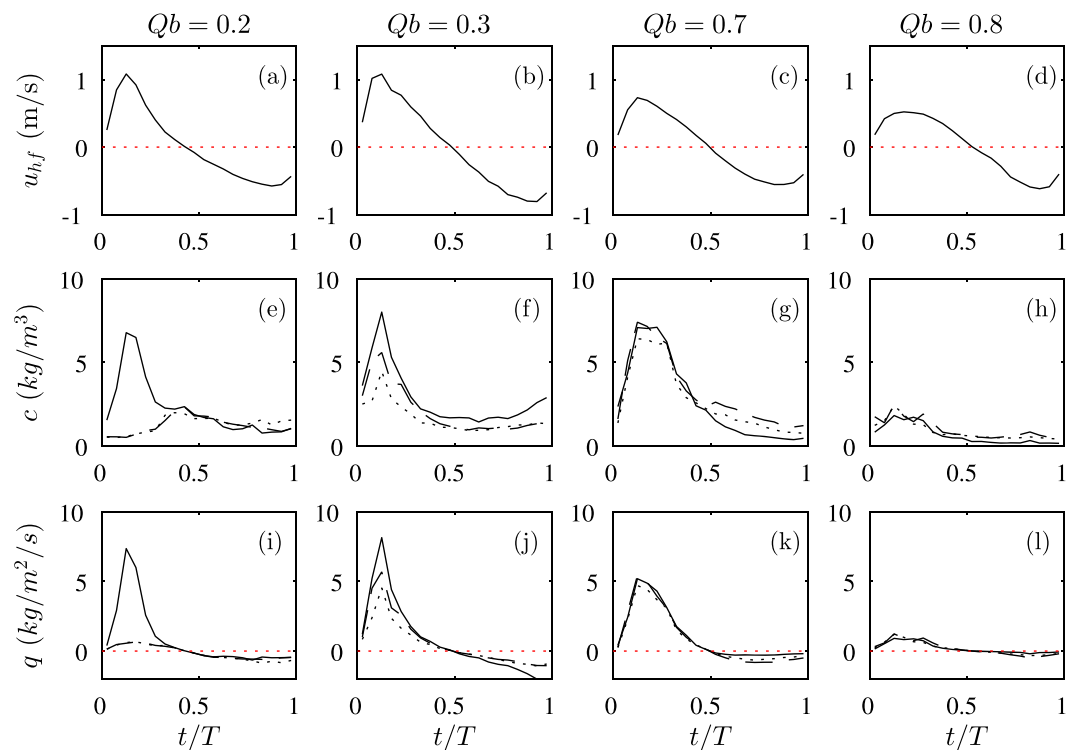


**Figure 8.** Phase-averaged (a–d)  $u_{hf}$ , (e–h)  $c$ , and (i–l)  $q$  at (solid line)  $z = 0.04$ , (dashed line)  $z = 0.07$  and (dotted line)  $z = 0.10$  m, at the four rigs in the surf zone during test C1, run 2 or 3.

significance for sand entrainment during our experiment is not clear from the pattern in phase coupling, as the phase-averaged concentration only peaks during positive flow which has been observed in the field both above ripples [Austin and Masselink, 2008] and above a flat bed [Black and Vincent, 2001].

For increasing  $H_s/h$ , the peak in phase-averaged suspension close to the bed ( $z = 0.04$  m) shifts from  $t/T \approx 0.3$  to  $t/T \approx 0.15$  (Figure 6b), i.e., the suspension maximum gradually shifts from occurring just after the maximum positive  $u_{hf}$  to slightly before maximum positive  $u_{hf}$  when the wave-orbital motion becomes more asymmetric. Phase-averaged  $c$  at  $z \approx 0.11$  m shows considerably more scatter, which might be caused by differences in ripple characteristics (Figure 6d), indicating  $H_s/h$  does not explain all variability (Figure 6c). The general trend, however, is a decrease in phase lag between  $u_{hf}$  and  $c$  when  $H_s/h$  increases, from 0.3 when  $H_s/h = 0.2$  to 0 when  $H_s/h = 1$ . This implies that the difference in phase coupling of  $c$  with  $u_{hf}$  in the vertical disappears when  $H_s/h$  increases. An example at TR from the wave run with the lowest water level shows the maximum of the

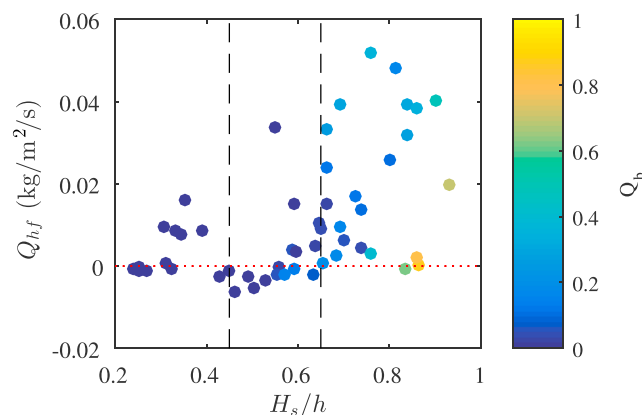


**Figure 9.** The cumulative high-frequency transport  $Q_{hf}$  versus relative wave height  $H_s/h$ . The colors indicate the fraction of broken waves  $Q_b$ .

phase-averaged  $c$  is present at the same  $t/T$  throughout the measured vertical transect ( $z \approx 0.04 - 0.17$  m, Figure 7f). The phase-averaged  $k$  for these measurements from the surf zone is an order of magnitude larger than beneath nonbreaking waves and shows the highest value beneath the front of the waves (Figure 7d). This probably represents the injection of turbulence by the plunging breakers.

Besides the differences in terms of phase coupling beneath nonbreaking and breaking waves, the nonnormalized phase-averaged concentration beneath nonbreaking waves also shows a decrease in concentration vertically upward and a more homogeneous concentration beneath breaking waves (Figures 7c and 7d). The concentration close to the bed,  $z \approx 0.04$  m, beneath nonbreaking waves is of the same magnitude as beneath breaking waves (Figures 7e and 7f and 8e and 8f). To explore the nonnormalized phase-averaged concentration for the outer surf and inner surf, Figure 8 shows the cross-shore evolution of phase-averaged  $u_{\text{hf}}$ ,  $c$ , and  $q$  during two runs of C1 with a low water level and  $Q_b = 0.2-0.8$ . For each location, run 2 or 3 was chosen depending on which run passed the checks on air bubbles (section 2.2). At R1, where  $Q_b = 0.2$ , measured  $c$  shows a phase lag in the vertical, with maximum phase-averaged  $c$  at the higher sensors during positive to negative flow reversal, as was earlier also seen for lower  $Q_b$  values. During those conditions,  $q_{\text{hf}}$  is only of importance close to the bed (Figure 8i). As  $Q_b$  increases to 0.3, the phase lag between the concentration time series in the vertical approaches zero. Further shoreward ( $Q_b = 0.7$ ), the concentration peak widens but remains high throughout the positive flow phase of the waves (Figure 8g). With increasing distance from the onset of wave breaking, well into the inner-surf zone with  $Q_b \sim 0.8$ , the amount of sand suspended in the water column decreases at all heights but the phase coupling and thus the sand transport direction remain unaltered (Figures 8h and 8l).

The net effect of different phase coupling within the wave phase and in the vertical leads to a dependence of the cumulative high-frequency transport  $Q_{\text{hf}}$  on  $H_s/h$ . As discussed previously, the phase lag increases and sand concentration decreases vertically upward for low  $H_s/h$ . Hence,  $Q_{\text{hf}}$  is around zero for  $H_s/h < 0.65$  (Figure 9). Below plunging waves, sand is suspended during the onshore wave-orbital motion throughout the vertical measurement transect. Hence,  $Q_{\text{hf}}$  is positive and substantially larger in the outer-surf zone ( $0.6 < H_s/h < 1.0$ ). Further shoreward, in the inner-surf zone ( $Q_b > 0.5$ ), the transport decreases as sand concentrations decrease (Figure 9). This implies that the largest onshore  $Q_{\text{hf}}$  is found in the outer-surf zone.

#### 4. Discussion

The fraction of related events in the surf zone is relatively high (both  $E_{k|c}$  and  $E_{c|k}$ ) compared to the data of Yoon and Cox [2012]. This indicates that turbulence beneath plunging breakers is more effective in stirring sand from the bed than the turbulence beneath spilling breakers in their experiments. Although the related event fractions are high, in none of the tests all suspension events are related to turbulence or vice versa. This can, at least partly, be explained by the instruments measuring in one location. It is very well possible that suspension events were generated by measured turbulence events but were missed by the STMs or vice versa. Visual observations in detailed small-scale laboratory experiments showed that sand suspension is strongly three-dimensional [e.g., Nadaoka et al., 1988]. Irrespective of the causes, it is obvious that individual sand suspension events cannot be predicted deterministically from turbulence information alone, see also Yoon et al. [2013]. Therefore, the results of a more stochastic approach, i.e., averaging in the wave phase, were subsequently evaluated.

We acknowledge that the wave-induced sand transport is not represented by the suspended load transport alone, and bed load transport can under specific conditions also significantly contribute. Miles and Thorpe [2015] discussed the relative importance of bed load transport using field measurements of bed form migration rates, which are shown to give a good representation of the bed load transport under conditions when sheet flow is not of importance [Traykovski et al., 1999]. The bed form contribution to the total transport in their measurements varied highly between individual cases but was around 15% if averaged over the cross shore. Migration rates are driven by nonlinearities in the wave-orbital motion [Masselink et al., 2007; Miles and Thorpe, 2015] and are therefore part of the total wave-induced transport. Bed forms were not observed to migrate in a specific direction during the cases discussed in this study [Ruessink et al., 2015], and the suspended load transport thus explains the bulk of the total wave-induced sand transport.

Earlier measurements beneath velocity-asymmetric flows in oscillatory flow tunnels [van der A et al., 2009; Ruessink et al., 2011] show high sand concentration during both the positive and negative flow phase. Beneath the plunging breakers and bores in our study, sand is predominantly suspended during the onshore

wave-orbital motion. For the plunging breakers this can be ascribed to the injection of turbulence at the wavefront, this strong phase coupling of turbulence with the wave-orbital motion was also seen in other laboratory studies [e.g., *Ting and Kirby*, 1994; *van der Zanden et al.*, 2016]. There is, however, less agreement on the existence of phase coupling in the inner-surf zone. Several studies, both in the laboratory and in the field, suggest that sand suspension becomes unrelated to the wave-orbital motion beneath surf bores [e.g., *Nadaoka et al.*, 1988; *Barkaszi and Dally*, 1992; *Aagaard and Hughes*, 2010], while in our measurements and the field measurements by *Yu et al.* [1993] sand suspension occurred predominantly beneath the crest of the bores. This difference might be explained by the breaker type from which the bores originate, as *Ting and Kirby* [1995, 1996] describe that turbulence is more homogeneous beneath bores that originate from spilling breakers. *Ting and Kirby* [1994] ascribe this difference to the higher  $H_s/h$  present beneath bores that originate from plunging breakers. This means that for the same  $h$ , plunging breaker bores are higher and can thus be more effective in stirring sand. This hypothesis is in agreement with the breaker types during the experiments of *Nadaoka et al.* [1988] (spilling breakers) and *Yu et al.* [1993] (plunging breakers), but it is difficult to compare all measurements as information on the exact location of the instruments with respect to the breakpoint is often not provided.

In this study we have shown the differences between sand suspension under nonbreaking and breaking irregular waves, with fraction of breaking waves between  $Q_b = 0$  and  $Q_b = 0.8$ . Overall, when  $H_s/h$  and  $Q_b$  increase, turbulence becomes more effective in stirring sand from the bed and simultaneously reduces the phase lag in the vertical between the wave-orbital motion and concentration. The wave-induced sand transport in current morphodynamic models is often solely based on the wave-orbital motion and thus lack the effect of surface-induced turbulence. Most of these models now need site-specific calibration through free model parameters [e.g., *Ruessink et al.*, 2007; *Walstra et al.*, 2012; *Dubarbier et al.*, 2015] to compensate for the lack of certain physical processes. In this study we show that sand suspension is strongly coupled to the onshore phase of the wave-orbital motion beneath plunging breakers and bores. This signifies that the onshore-driven sand transport in the surf zone is significantly higher when the effect of surface-induced turbulence is included. In future work we will determine the relative importance of  $Q_{hf}$  to the total sand transport.

#### Acknowledgments

We would like to acknowledge everyone who contributed to the BARDEX II experiments, particularly Florent Grasso, Daan Wesselman, and Winnie de Winter for the collection of the data used in this study and Marcel van Maarsseveen, Henk Markies, and the Deltares Delta Flume staff for the technical support. Furthermore, we would like to thank Jantien Rutten and Timothy Price for the many discussions during the data interpretation phase and three anonymous reviewers, Associate Editor Curt Storlazzi, and Editor Giovanni Coco for their constructive comments on the manuscript. BARDEXII was supported by the European Community's 7th Framework Programme through the grant to the budget of Integrating Activity HYDRALAB IV, contract 261520. J.A.B. and B.G.R. were funded by the Dutch Technology Foundation STW, which is part of the Netherlands Organization for Scientific Research (NWO), and is partly funded by the Ministry of Economic Affairs (project number 12397). A.T.M.d.B. acknowledges funding by the NWO under contract 821.01.012. The data used in this study can be made available upon request from the first author.

#### 5. Conclusions

Measurements of near-bed turbulence, wave-orbital motion, sand concentration, and ripple characteristics were collected beneath irregular waves in the shoaling and surf zone of a field-scale laboratory beach. Event-by-event analysis shows that turbulence beneath plunging breaking waves with subdued ripples is more effective in stirring sand from the bed than turbulence beneath nonbreaking shoaling waves above vortex ripples. Although turbulence events can be correlated to about 50% of the suspension events, the origin of a large part of the suspension events remains unclear.

Below nonbreaking waves, sand is brought into suspension right after the maximum positive wave-orbital motion  $u_{hf}$  and reaches higher elevations during flow reversal from positive to negative  $u_{hf}$ . This is substantially different from the suspension pattern beneath breaking waves and bores, where phase-averaged  $c$  peaks during the positive-directed wave-orbital motion throughout the measured part of the water column. In the inner-surf zone  $c$  remains phase coupled to the wave-orbital motion, but the concentration decreases with distance from the onset of wave breaking.

The vertically integrated suspended sand transport by short waves  $Q_{hf}$  is thus onshore and largest beneath plunging waves. Under bores in the inner surf,  $Q_{hf}$  remains onshore but is smaller, while under shoaling waves  $Q_{hf}$  is smallest and can also be offshore directed. To accurately predict the contribution of short, breaking (plunging) waves to the total suspended sand transport in morphodynamic models, the effect of the injection of surface-induced turbulence on short-wave sand transport should thus be included.

#### References

- Aagaard, T., and M. G. Hughes (2010), Breaker turbulence and sediment suspension in the surf zone, *Mar. Geol.*, 271(3–4), 250–259, doi:10.1016/j.margeo.2010.02.019.
- Aagaard, T., and S. G. Jensen (2013), Sediment concentration and vertical mixing under breaking waves, *Mar. Geol.*, 336, 146–159, doi:10.1016/j.margeo.2012.11.015.
- Aagaard, T., B. Greenwood, and M. Hughes (2013), Sediment transport on dissipative, intermediate and reflective beaches, *Earth Sci. Rev.*, 124, 32–50, doi:10.1016/j.earscirev.2013.05.002.

- Austin, M. J., and G. Masselink (2008), The effect of bedform dynamics on computing suspended sediment fluxes using optical backscatter sensors and current meters, *Coastal Eng.*, *55*(3), 251–260, doi:10.1016/j.coastaleng.2007.10.003.
- Barkaszi, S. F., and W. R. Dally (1992), Fine-scale measurement of sediment suspension by breaking waves at Supertank, in *Proceedings of the 23rd International Coastal Engineering Conference*, pp. 1910–1923, ASCE, Venice, Italy.
- Beach, R. A., and R. W. Sternberg (1996), Suspended-sediment transport in the surf zone: Response to breaking waves, *Cont. Shelf Res.*, *16*(15), 1989–2003.
- Black, K., and C. Vincent (2001), High-resolution field measurements and numerical modelling of intra-wave sediment suspension on plane beds under shoaling waves, *Coastal Eng.*, *42*(2), 173–197, doi:10.1016/S0378-3839(00)00058-2.
- Brinkkemper, J. A., T. Lanckriet, F. Grasso, J. A. Puleo, and B. G. Ruessink (2016), Observations of turbulence within the surf and swash zone of a field-scale sandy laboratory beach, *Coastal Eng.*, *113*, 62–72, doi:10.1016/j.coastaleng.2015.07.006.
- Butt, T., P. Russell, J. Puleo, J. Miles, and G. Masselink (2004), The influence of bore turbulence on sediment transport in the swash and inner surf zones, *Cont. Shelf Res.*, *24*(7–8), 757–771, doi:10.1016/j.csr.2004.02.002.
- Cox, D. T., and N. Kobayashi (2000), Identification of intense, intermittent coherent motions under shoaling and breaking waves, *J. Geophys. Res.*, *105*(C6), 14,223–14,236, doi:10.1029/2000JC900048.
- de Winter, W., D. Wesselman, F. Grasso, and G. Ruessink (2013), Large-scale laboratory observations of beach morphodynamics and turbulence beneath shoaling and breaking waves, *J. Coastal Res.*, *2*(65), 1515, doi:10.2112/SI65-256.1.
- Dohmen-Janssen, C. M., D. F. Kroekenstoel, W. N. Hassan, and J. S. Ribberink (2002), Phase lags in oscillatory sheet flow: Experiments and bed load modelling, *Coastal Eng.*, *46*(1), 61–87, doi:10.1016/S0378-3839(02)00056-X.
- Dubarbier, B., B. Castelle, V. Marieu, and G. Ruessink (2015), Process-based modeling of cross-shore sandbar behavior, *Coastal Eng.*, *95*, 35–50, doi:10.1016/j.coastaleng.2014.09.004.
- Elgar, S. (1987), Relationships involving third moments and bispectra of a harmonic process, *IEEE Trans. Acoust. Speech Signal Process.*, *35*(12), 1725–1726.
- Elgar, S., B. Raubenheimer, and R. T. Guza (2005), Quality control of acoustic Doppler velocimeter data in the surfzone, *Meas. Sci. Technol.*, *16*(10), 1889–1893, doi:10.1088/0957-0233/16/10/002.
- Feddersen, F., and A. J. Williams (2007), Direct estimation of the Reynolds stress vertical structure in the nearshore, *J. Atmos. Oceanic Technol.*, *24*(1), 102–116, doi:10.1175/JTECH1953.1.
- Gerbi, G. P., J. H. Trowbridge, E. A. Terray, A. J. Plueddemann, and T. Kukulka (2009), Observations of turbulence in the ocean surface boundary layer: Energetics and transport, *J. Phys. Oceanogr.*, *39*(5), 1077–1096, doi:10.1175/2008JPO4044.1.
- Grasso, F., H. Michallet, and E. Barthélemy (2011), Sediment transport associated with morphological beach changes forced by irregular asymmetric, skewed waves, *J. Geophys. Res.*, *116*, C03020, doi:10.1029/2010JC006550.
- Jaffe, B., and A. Sallenger Jr. (1992), The contribution of suspension events to sediment transport in the surf zone, in *Proceedings of the 23rd International Coastal Engineering Conference*, vol. 3, pp. 2680–2693, ASCE, Venice, Italy.
- Jaffe, B. E., R. W. Sternberg, and A. H. Sallenger (1984), The role of suspended sediment in shore-normal beach profile changes, *Coastal Eng. Proceedings*, *1*(19).
- King, D. B. (1991), Studies in oscillatory flow bedload sediment transport, PhD thesis, Univ. of Calif., San Diego.
- Masselink, G., M. J. Austin, T. J. O'Hare, and P. E. Russell (2007), Geometry and dynamics of wave ripples in the nearshore zone of a coarse sandy beach, *J. Geophys. Res.*, *112*, C10022, doi:10.1029/2006JC003839.
- Masselink, G., A. Ruju, D. Conley, I. Turner, G. Ruessink, A. Matias, C. Thompson, B. Castelle, and G. Wolters (2016), Large-scale barrier dynamics experiment II (BARDEX II): Experimental design, instrumentation, test programme and data set, *Coastal Eng.*, *113*, 3–18, doi:10.1016/j.coastaleng.2015.07.009.
- Miles, J., and A. Thorpe (2015), Bedform contributions to cross-shore sediment transport on a dissipative beach, *Coastal Eng.*, *98*, 65–77, doi:10.1016/j.coastaleng.2015.01.007.
- Mori, N., T. Suzuki, and S. Kakuno (2007), Noise of acoustic Doppler velocimeter data in bubbly flows, *J. Eng. Mech.*, *133*(1), 122–125, doi:10.1061/(ASCE)0733-9399(2007)133:1(122).
- Nadaoka, K., S. Ueno, and T. Igarashi (1988), Sediment suspension due to large scale eddies in the surf zone, in *Proceedings of the 21st International Conference on Coastal Engineering*, pp. 1646–1660, ASCE, Malaga, Spain.
- Nadaoka, K., M. Hino, and Y. Koyano (1989), Structure of the turbulent flow field under breaking waves in the surf zone, *J. Fluid Mech.*, *204*, 359–387.
- Nielsen, P. (1992), *Coastal Bottom Boundary Layers and Sediment Transport: Advanced Series on Ocean Engineering*, World Sci. Publ. Co., Singapore.
- O'Donoghue, T., and S. Wright (2004), Flow tunnel measurements of velocities and sand flux in oscillatory sheet flow for well-sorted and graded sands, *Coastal Eng.*, *51*(11–12), 1163–1184, doi:10.1016/j.coastaleng.2004.08.001.
- Osborne, P. D., and B. Greenwood (1992), Frequency dependent cross-shore suspended sediment transport. 2. A barred shoreface, *Mar. Geol.*, *106*(1–2), 25–51.
- Osborne, P. D., and C. E. Vincent (1996), Vertical and horizontal structure in suspended sand concentrations and wave-induced fluxes over bedforms, *Mar. Geol.*, *131*, 195–208.
- Plant, N. G., K. T. Holland, and J. A. Puleo (2002), Analysis of the scale of errors in nearshore bathymetric data, *Mar. Geol.*, *191*, 71–86, doi:10.1016/S0025-3227(02)00497-8.
- Puleo, J. A. (2009), Tidal variability of swash-zone sediment suspension and transport, *J. Coastal Res.*, *25*(4), 937–948, doi:10.2112/08-1031.1.
- Puleo, J. A., R. V. Johnson, T. Butt, T. N. Kooney, and K. T. Holland (2006), The effect of air bubbles on optical backscatter sensors, *Mar. Geol.*, *230*(1), 87–97, doi:10.1016/j.margeo.2006.04.008.
- Ribberink, J. S., and A. A. Al-Salem (1994), Sediment transport in oscillatory boundary layers in cases of rippled beds and sheet flow, *J. Geophys. Res.*, *99*(C6), 12,707–12,727.
- Ruessink, B. G. (2010), Observations of turbulence within a natural surf zone, *J. Phys. Oceanogr.*, *40*(12), 2696–2712, doi:10.1175/2010JPO4466.1.
- Ruessink, B. G., K. T. Houwman, and P. Hoekstra (1998), The systematic contribution of transporting mechanisms to the cross-shore sediment transport in water depths of 3 to 9 m, *Mar. Geol.*, *152*, 295–324.
- Ruessink, B. G., Y. Kuriyama, A. J. H. M. Reniers, J. A. Roelvink, and D. J. R. Walstra (2007), Modeling cross-shore sandbar behavior on the timescale of weeks, *J. Geophys. Res.*, *112*, F03010, doi:10.1029/2006JF000730.
- Ruessink, B. G., T. J. J. van den Berg, and L. C. van Rijn (2009), Modeling sediment transport beneath skewed asymmetric waves above a plane bed, *J. Geophys. Res.*, *114*, C11021, doi:10.1029/2009JC005416.
- Ruessink, B. G., H. Michallet, T. Abreu, F. Sancho, D. A. Van der A, J. J. Van der Werf, and P. A. Silva (2011), Observations of velocities, sand concentrations, and fluxes under velocity-asymmetric oscillatory flows, *J. Geophys. Res.*, *116*, C03004, doi:10.1029/2010JC006443.

- Ruessink, B. G., J. A. Brinkkemper, and M. G. Kleinhans (2015), Geometry of wave-formed orbital ripples in coarse sand, *J. Marine Sci. Eng.*, 3(4), 1568–1594, doi:10.3390/jmse3041568.
- Ruessink, B. G., C. Blenkinsopp, J. A. Brinkkemper, B. Castelle, B. Durbarbier, F. Grasso, J. A. Puleo, T. Lanckriet, and G. Masselink (2016), Sandbar and beachface evolution on a prototype coarse-grained sandy barrier, *Coastal Eng.*, 113, 19–32, doi:10.1016/j.coastaleng.2015.11.005.
- Sato, S., K. Homma, and T. Shibayama (1990), Laboratory study on sand suspension due to breaking waves, *Coastal Eng. Jpn.*, 33(2), 219–231.
- Scott, N. V., T.-J. Hsu, and D. Cox (2009), Steep wave, turbulence, and sediment concentration statistics beneath a breaking wave field and their implications for sediment transport, *Cont. Shelf Res.*, 29(20), 2303–2317, doi:10.1016/j.csr.2009.09.008.
- Thorne, P. D., A. G. Davies, and J. J. Williams (2003), Measurements of near-bed intra-wave sediment entrainment above vortex ripples, *Geophys. Res. Lett.*, 30(20), 2028, doi:10.1029/2003GL018427.
- Ting, F. C. K., and J. T. Kirby (1994), Observation of undertow and turbulence in a laboratory surf zone, *Coastal Eng.*, 24(1–2), 51–80.
- Ting, F. C. K., and J. T. Kirby (1995), Dynamics of surf-zone turbulence in a strong plunging breaker, *Coastal Eng.*, 24(3–4), 177–204.
- Ting, F. C. K., and J. T. Kirby (1996), Dynamics of surf-zone turbulence in a spilling breaker, *Coastal Eng.*, 27(3–4), 131–160.
- Traykovski, P., A. E. Hay, J. D. Irish, and J. F. Lynch (1999), Geometry, migration, and evolution of wave orbital ripples at LEO-15, *J. Geophys. Res.*, 104(C1), 1505–1524.
- van der A, D. A., T. O'Donoghue, and J. S. Ribberink (2009), Sheet flow sand transport processes in oscillatory flow with acceleration skewness, in *Paper 133 in Proceedings Coastal Dynamics '09*, 1–15, Tokyo.
- van der A, D. A., T. O'Donoghue, and J. S. Ribberink (2010), Measurements of sheet flow transport in acceleration-skewed oscillatory flow and comparison with practical formulations, *Coastal Eng.*, 57(3), 331–342, doi:10.1016/j.coastaleng.2009.11.006.
- van der Werf, J. J., J. S. Doucette, T. O'Donoghue, and J. S. Ribberink (2007), Detailed measurements of velocities and suspended sand concentrations over full-scale ripples in regular oscillatory flow, *J. Geophys. Res.*, 112, F02012, doi:10.1029/2006JF000614.
- van der Zanden, J., D. van der A, D. Hurther, I. Cáceres, T. O'Donoghue, and J. Ribberink (2016), Near-bed hydrodynamics and turbulence below a large-scale plunging breaking wave over a mobile barred bed profile, *J. Geophys. Res. Oceans*, 121, 6482–6506, doi:10.1002/2016JC011909.
- Van Rijn, L. C., J. S. Ribberink, J. Van Der Werf, and D. J. R. Walstra (2013), Coastal sediment dynamics: Recent advances and future research needs, *J. Hydraul. Res.*, 51(5), 475–493, doi:10.1080/00221686.2013.849297.
- van Thiel de Vries, J. S. M., M. R. A. Van Gent, D. J. R. Walstra, and A. J. H. M. Reniers (2008), Analysis of dune erosion processes in large-scale flume experiments, *Coastal Eng.*, 55(12), 1028–1040, doi:10.1016/j.coastaleng.2008.04.004.
- Walstra, D., A. Reniers, R. Ranasinghe, J. Roelvink, and B. Ruessink (2012), On bar growth and decay during interannual net offshore migration, *Coastal Eng.*, 60, 190–200, doi:10.1016/j.coastaleng.2011.10.002.
- Yoon, H.-D., and D. T. Cox (2012), Cross-shore variation of intermittent sediment suspension and turbulence induced by depth-limited wave breaking, *Cont. Shelf Res.*, 47, 93–106, doi:10.1016/j.csr.2012.07.001.
- Yoon, H.-D., D. T. Cox, and M. Kim (2013), Prediction of time-dependent sediment suspension in the surf zone using artificial neural network, *Coastal Eng.*, 71, 78–86, doi:10.1016/j.coastaleng.2012.08.005.
- Yu, Y., R. W. Sternberg, and R. A. Beach (1993), Kinematics of breaking waves and associated suspended sediment in the nearshore zone, *Cont. Shelf Res.*, 13(11), 1219–1242.
- Zhang, D., and T. Sunamura (1990), Conditions for the occurrence of vortices induced by breaking waves, *Coastal Eng. Jpn.*, 33(2), 145–155.